# Buried moiré supercells through SrTiO₃ nanolayer relaxation

Max Burian,[*] Bill Francesco Pedrini, Nazaret Ortiz Hernandez ⬤, Hiroki Ueda ⬤, C. A. F. Vaz ⬤, Marco Caputo,
Milan Radovic, and Urs Staub ⬤[†]

*Swiss Light Source, Paul Scherrer Institute, 5232 Villigen PSI, Switzerland*

We identified a highly ordered moiré lattice at the buried SrTiO₃ (STO)-(La,Sr)(Al,Ta)-oxide (LSAT) interface by high-resolution x-ray diffraction reciprocal space mapping. We found long-ranged ordered supercells of 106/107 unit cells of unstrained STO-LSAT caused by complete lattice relaxation through high-temperature annealing. Transmission electron microscopy images show that this periodicity is based on line dislocations at the interface region. The presence of such ordered superstructures in such widely used complex oxides sets the ideal conditions for moiré-tuned interfacial electronic modifications and ferroelectric supercrystallinity, opening the possibility for interface functionalities and impacting findings on vortex structured multilayers systems.

Complex oxide heterostructures with their unique set of physical and chemical properties are of looming interest for magneto-electronic devices [1–8]. Intrinsic material properties, such as (i) spin-interactions [9], (ii) strong multiferroric character [10], and (iii) high thermal and operational stability [11], are extended by electronic interactions at the heterointerface [8,12–14]. Indeed, accurate interface engineering has led to a new functional repertoire [15], including observations of quasi-two-dimensional (2D) electron gas (2DEG) [14,16,17], charge writing [18], resistance switching [19], occurrence of electronic [20] and magnetic order [21], giant thermoelectric effect [22], and colossal ionic conductivity [23]. The origins of these collective phenomena lie in site-specific spin and charge interactions [24–26] that are in turn governed by the local atomic arrangement [27]. Indeed, simple misalignment of two equal lattices induces a long-range ordered superstructure termed "moiré motif" that manifests itself in new collective properties, e.g., plasmonic minibands [28] or moiré excitons [29]. Precise knowledge of the atomic structure at the interface, even between seemingly equal lattices, is hence key to understand and enhance the collective material system behavior.

Prominent candidates for such oxide-based heterostructures are perovskite titanates, including SrTiO₃ (STO) that presents an exceptional high and tunable dielectric constant [30,31]. Quantum fluctuations of the cell-centered Ti-atom suppress the paraelectric-to-ferroelectric transition [32], whereas these fluctuations are driven by the STO soft phonon mode [33]. Lattice straining effects that drastically alter the respective phonon modes therefore determine the dielectric anisotropy of the material, which plays a crucial role in heterostructures of STO, leading either to (i) a polar structure [34,35] or to (ii) suppression of lattice polarizability and strong reduction in dielectric character [31,36]. Obtaining ideal bulk material properties in STO films hence requires perfect relaxation of the crystalline lattice by structural decoupling from the substrate. Indeed, this lattice relaxation might also be crucial for the occurrence of ferroelectric three-dimensional (3D) vortex structures [37,38], room temperature skyrmion structures [39], or laser-induced supercrystallinity [40] in STO-based nanolayer heterostructures, yet the structural origin of these phenomena is not fully understood.

Here, we look at the interface between a nanolayer of STO grown on a $(LaAlO_3)_{0.3}(Sr_2TaAlO_6)_{0.7}$ (LSAT) substrate. Both compounds have a cubic lattice ($a_{STO} = 3.905$ Å [41]; $a_{LSAT} = 3.869$ Å [42]) and a mismatch of +0.93%. Despite this small lattice mismatch, straining from lattice matching of the grown STO layer is sufficient to suppress the soft phonon mode [32,43]. As previously shown, one can recover the bulklike phononic landscape by high temperature annealing in ambient atmosphere [32,43] for a 82 nm thick film, suggesting structural relaxation of the STO nanolayer, in contrast to an ultrathin 8.2 nm thick film. We follow this approach and use a ∼30 nm thick film of STO on LSAT (001) grown by pulsed laser deposition, followed by 12 h of annealing at 1200°C at ambient atmosphere [43]. We find that this heat treatment leads to complete relaxation of the STO nanolayer, resulting in a moiré pattern at the STO-LSAT interface. Comparison with theoretical calculations shows that this moiré interference occurs if the atomic bond length at the interface varies. Indeed, the atomic displacements at the interface correspond to a highly ordered network of line dislocations, as observed by high resolution transmission electron microscopy (HRTEM). Our explanation not only helps to understand recent reports of 3D vortex structures [37–40] but also implies a long-range ordered modulation of the interfacial electronic states [44], opening applicative perspectives for 2D ferroics.

---

[*]max.burian@psi.ch
[†]urs.staub@psi.ch

The STO on LSAT film is the same as in Ref. [43]. X-ray diffraction (XRD) experiments were performed at the surface XRD (SXRD) endstation of the MS beamline [45,46] at the Swiss Light Source. The x-ray beam (12.65 keV) was focused and cut to a beam size of $500 \times 500 \ \mu$m ($H$ x $V$) at the sample, which was mounted on a $(2 + 3)$-type surface diffractometer (vertical geometry) [47] with an angular resolution of $0.002°$. During scans, the intensity of the incident beam is automatically adjusted (by a variable transmission-filter array) to optimize the effective dynamic range of each scan. The orientation-matrix describing sample alignment in the beamline coordinate system was defined by manual alignment of three nonorthogonal and two orthogonal reflections, resulting in an accuracy of $h, k, l \pm 0.0005$ reciprocal lattice units (r.l.u.). Reciprocal space scans (200 images, 1 s each) over each reflection were made along the [001] and [112] directions to check for possible distortion or misalignment effects. Angular-to-reciprocal space conversion of each detector pixel was done according to Schlepütz *et al.* [47]. For each scan, an array of all 3D reciprocal space coordinates with the corresponding scattering intensities were interpolated onto an orthogonal, equidistant (voxel size $h, k, l = 0.0005$ r.l.u) 3D matrix, constituting the reciprocal space volume (RSV). The convolution product of (i) experimental accuracy and (ii) the RSV voxel size yields the effective resolution of the RSV, which in this case is $h, k, l \pm 0.0007$ r.l.u. RSVs are transferred into the STO-*HKL* space [named indices relate to STO where capital indices (e.g., $H$, $K$, or $L$) denote reference positions in reciprocal space, while lowercase indices (e.g., $h$, $k$, or $l$) denote scanning variables]. A detailed description of the fast Fourier transform (FFT) model calculations can be found in Appendices C and D on 2D and 3D model calculations, respectively. Samples for transmission electron microscopy were prepared in cross-section geometry parallel to the (100) planes of the LSAT substrate by means of a FEI Helios NanoLab 600i focused ion beam instrument operated at 30 and 5 kV accelerating voltages. High angle annular dark-field scanning transmission electron microscopy was performed using a FEI Titan Themis microscope equipped with a hexapole-type probe spherical aberration corrector (CEOS DCOR) operated at 300 kV.

Since structural motifs of the hetero-interface are often projected onto the sample surface [48], we characterize the STO nanolayer morphology by atomic force microscopy (AFM), as detailed in Appendix A. As seen in Fig. 4(a), AFM shows disordered islands with 5–8 nm thickness and 146 nm mean lateral correlation length [see Figs. 4(b) and 4(c) for Fourier analysis of the AFM image]. Such an island pattern has been linked to segregation effects during annealing and is usually found to seed at lattice defects, such as dislocations and/or surface atomic steps [48–51]. The absence of a long-range ordered island arrangement (here evidenced by disorder) hence points towards an isotropic STO nanolayer morphology and gives no further information on the interface properties.

To obtain information on the atomic lattice strain state, we collect reciprocal space slices (scattering images) by synchrotron XRD, which we map and assemble into 3D RSVs. First, we select the low symmetry $(2, 0, L)$ family with $L = 2, 3$, and 4, which provides information on the out-of-plane strain state of the STO film. As shown in Fig. 1, we observe
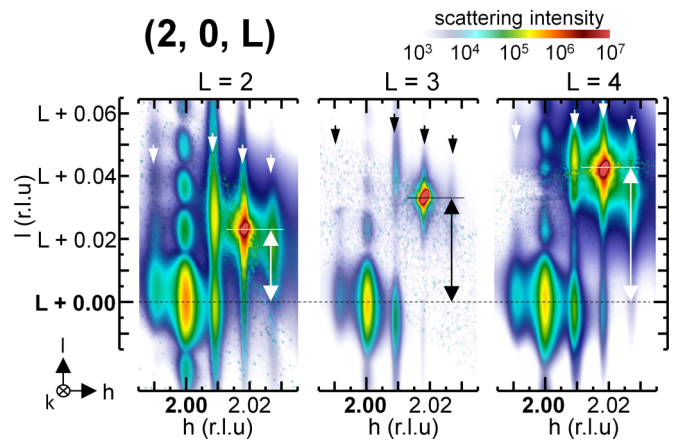


FIG. 1. Slices through the reciprocal space volume (RSV) obtained by x-ray diffraction (XRD) at the $(2, 0, L)$ family peaks. The reciprocal space distance between substrate and surface layer peak increases linearly with $L$ diffraction order, yielding an out-of-plane lattice difference of $1.07 \pm 0.10\%$. The scattering intensity is scaled logarithmically according to the color bar.

rodlike scattering features extending along the $l$ axis, typical for nanolayers. For all Bragg peaks, oscillations at $k = 0$ along $l$ can be observed, corresponding to layer thickness-dependent fringes [see rocking curve in Fig. 5(a), confirming a STO film thickness of $33 \pm 3$ nm]. For more information, see Appendix B. More evidently, the RSV presents two significant scattering contributions along the $l$ direction, from (i) the layer (at lower $l$) and (ii) the substrate (at higher $l$). From the distance between the two scattering centers, we calculate the difference in out-of-plane $d$ spacing of STO and LSAT, yielding a mismatch of $+1.07 \pm 0.10\%$. This value is only slightly above the theoretical prediction for a perfectly relaxed lattice $(+0.93\%)$.

Interestingly, the scattering rods, seen as streaks along the out-of-plane $l$ direction (see Fig. 1), present repetitions along the in-plane $k$ direction. Note that the small distance between these rods in reciprocal space must relate to a large period in real space. Indeed, such scattering features are characteristic of a large-scale and long-range order as found in superstructures [20,52–54], here relating to an in-plane $d$ spacing of 41.1 nm (reciprocal space distance of $\Delta k = 0.0096$ r.l.u. between the modulations—see Figs. 5 and 6 for peak fits). Interestingly, the scattering rods appear to be commensurate with the atomic LSAT and STO Bragg reflections, as both peaks (of an $H = 2$ type reflection) are linked by exactly two scattering rods.

To understand if there indeed exists a relation between the scattering rods and the underlying atomic lattices, we vary the in-plane index within the same $(2, K, 4)$ family, as shown in Fig. 2(a). Remarkably, by varying $k$ between $-2$ to 2, the substrate peak (at $l = 4.045$) and the STO peak (at $l = 4.00$) always fall on superstructure scattering rods. For example, at the $(2, -2, 4)$ reflection, the substrate peak lies on the second scattering rod from STO, whereas increasing $k$ to $-1$ translates the substrate peak to the neighboring rod. This effect becomes even clearer when looking at orthogonal projections that show the full in-plane relation [see Fig. 2(b)].
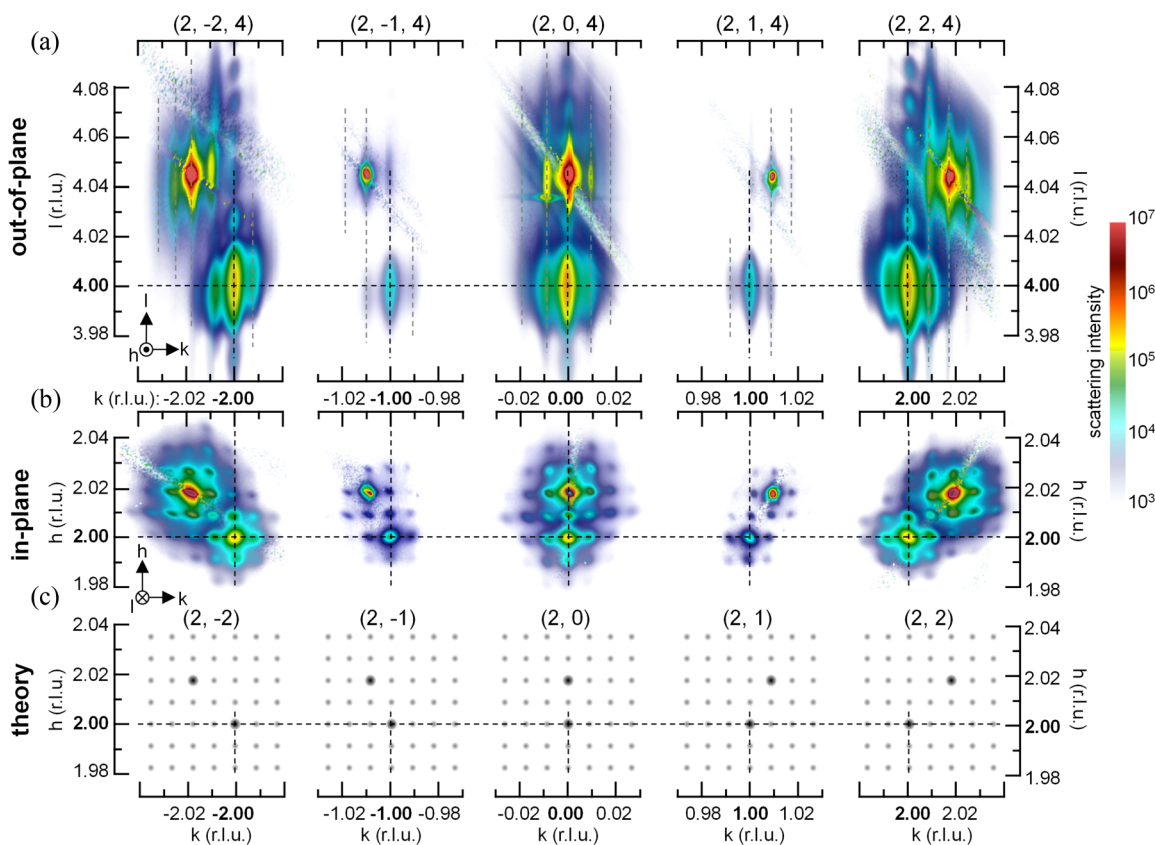
FIG. 2. (a) Out-of-plane and (b) in-plane sliced projections of the reciprocal space volume (RSV) obtained by x-ray scattering on the $(2, K, 4)$ family peaks, showing a commensurate relation between atomic lattice reflections and the superstructure scattering rods. Black dashed lines mark the center of the Bragg reflection in the SrTiO₃ (STO) reference frame. The scattering intensity is scaled logarithmically according to the color bar. (c) The intensity of two-dimensional (2D) Fourier transform of a theoretical 106/107 moiré lattice reproduces the same scattering behavior if an induced phase shift is considered.

At all reflections, the superstructure rods form an in-plane 2D lattice with square symmetry [see Figs. 5(b) and 5(c) for comparison of cuts along $h$ and $k$ trajectories]. Along $h$, substrate and layer peaks are always spaced two scattering rods apart (note that $H = 2$ for this reflection), while the substrate peak varies along $k$ on the 2D scattering rod grid with increasing diffraction order. This commensurate relation between atomic reflections and scattering rods therefore suggests a structural relation between the atomic crystalline lattices and the formed superstructure.

Regarding the origin of the observed scattering rods, it is important to realize that the superstructure scattering pattern is seen on both the substrate (LSAT) and layer (STO) peaks, implying that the underlying structural feature originates from the LSAT-STO interface. (We can rule out surface topology as the origin of the observed scattering rods, since we find a coherent domain size of the dislocation network >300 nm—see Fig. 6 for corresponding peak fits—which is significantly larger than the surface features with approximately 150 nm identified by AFM—see Fig. 4.) Further, the ratio between the STO lattice constant (3.905 Å) and the observed superstructure $d$ spacing (42.5 nm) corresponds to 0.92%, closely matching the theoretical STO-LSAT lattice mismatch of 0.93%. The observed scattering behavior hence stems from scattering interference of LSAT and the perfectly in-plane

relaxed STO layer, classified as a moiré-like motif [28,55,56]. In short, such moiré motifs appear through superposition of two (in this case square) base lattices with different periodicity $a_{small}$ and $a_{large}$, such that spatial interference gives rise to a new pattern with the same symmetry but a lattice constant of $a_{moire} = (a_{large} a_{small})/(a_{large} - a_{small})$ [57–59]. Here, these two base lattices relate to STO and LSAT, where it takes 106 unit cells of STO and 107 unit cells of LSAT to compensate the lattice mismatch of 0.93%, yielding a moiré lattice constant of 40.8 nm. Indeed, and as shown in Fig. 2(c), a 2D Fourier transform of such an idealized 106/107 Moiré lattice shows the same scattering motif as observed experimentally: the two strong reflections correspond to the original 106 and 107 base lattices, whereas the weak and smaller-spaced reflections correspond to the moiré interference terms (see Appendix C for a discussion on the origin of such superlattice reflections). Noteworthy, the periodicity of a 106/107 type moiré motif found here is 3–4 times larger than that reported for few layer such as graphene on boron-nitrite moiré systems [55,56,59–61].

The observation of such a moiré pattern allows us to draw conclusions about the LSAT-STO interface. First, it is evidence of an in-plane relaxed STO layer without remanent substrate-induced strain. Second, when moving along one of the principal crystallographic in-plane axes, one reaches a
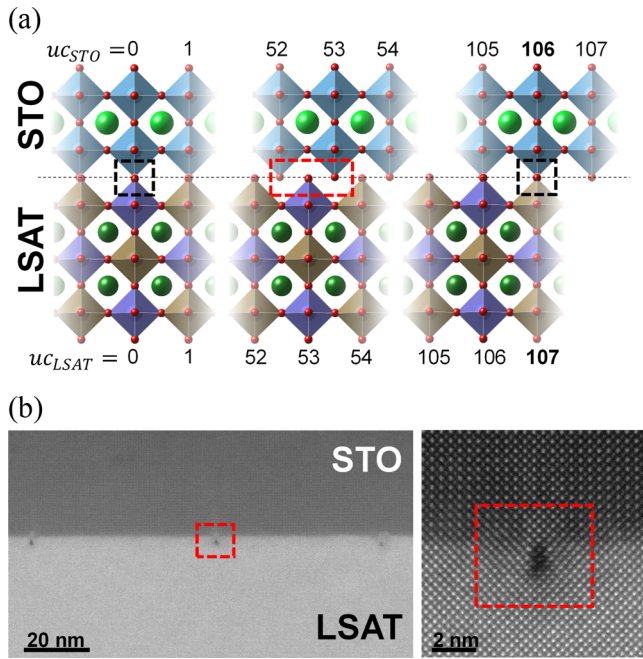
FIG. 3. (a) Structural illustration of the $SrTiO_3(STO) - (LaAlO_3)_{0.3}(Sr_2TaAlO_6)_{0.7}(LSAT)$ interface due to lattice relaxation, shown along the STO (100) direction. Starting from perfect overlap of the corresponding unit cells (uc; see black dashed area at $uc_{STO} = 0$), the local mismatch of the interfacial oxygen atoms increases until it is maximal at half the moiré periodicity (see red dashed area at $uc_{STO} = 53$). Eventually, the LSAT and STO unit cells overlap again (see black dashed area at $uc_{STO} = 106$), effectively forming a two-dimensional (2D) 106/107 moiré pattern. (b) High resolution transmission electron microscopy (HRTEM) images of the sample cross-section, showing a highly ordered arrangement (mean distance of 44.6 nm) of dislocations that form where the local mismatch is largest.

point of maximal local lattice mismatch [see Fig. 3(a)], setting the ideal energetic conditions for the formation of a line dislocation. Indeed, HRTEM images show a highly ordered arrangement of dislocations at the interface with similar periodicity (44.6 nm) as the moiré motif, as shown in Fig. 3(b) (note that a dislocation network has been observed, e.g., at the $(La_xSr_{1-x})MnO_3/LaAlO_3$ interface [62]). As shown in Fig. 3(a), this presence of recurring dislocations creates an in- and out-of-plane strain modulation that is maximal around the dislocation and negligible where the STO Ti-O-octahedra within a $106 \times 106$ square fall directly on top of LSAT (Ta;Al)-O-octahedra. Third, in contrast to pseudomorphic growth that induces bulk strain on the surface layer, the strain field around a dislocation is highly localized and decays with $\frac{1}{z}$ along the film thickness [63]. Indeed, when calculating the diffraction intensity of such a moiré pattern from a 3D sample, superstructure-reflections become visible if a repetitive in- or out-of-plane displacement as found for a line dislocation is taken into account—even if the displacement occurs only within the first two unit cells of the STO layer (see Appendix D for details). Notably, in case a 2DEG was initially present at the interface [44], it likely does not survive such an annealing process. However, it is known that

defect sites in STO show metallic conducting behavior [64]. Such a long-range ordered network of defects might therefore constitute the ideal environment for 2D grid conductivity at the interface. That this is likely a property of STO and not the substrate is shown by depositing a thin STO film on $NdGaO_3$, which (after the exact annealing step) shows the same type of superstructure and dislocations but with different lattice spacing due to the different lattice mismatch (see Fig. 9).

The concept of moiré motifs also helps to understand more complex structural arrangements, spanning over 3D. In a series of papers [37–40], x-ray superstructure reflections similar to the ones shown in this paper have been linked to the formation of 3D vortex structures in the heterostructured system of STO and $PbTiO_3$ (PTO) [Superlattices of $(STO)_n/(PTO)_n$ grown on 5 nm $SrRuO_3$ (SRO)-buffered $DyScO_3$ (DSO)]. In all cases, prominent superstructure scattering rods corresponding to real-space $d$ spacings of 9–11 nm have been observed, which are thought to arise from vortex-antivortex pairs of ferroelectric PTO. Without the need to understand the complex physics behind the vortex structures and considering the data presented in the paper by Stoica *et al.* [40] (showing that a single laser pump induces metastable ferroelectric domains with long-range order spanning over all three crystalline dimensions), we can now correlate the observations of these scattering rods within the framework of a simple moiré interference. In this sample system, PTO grows isomorph (yet slightly strained) on pseudocubic SRO ($a_{SRO} = 3.923$ Å) in one direction, yielding PTO in-plane lattice constants of $a_{PTO} = 3.929$ Å and $c_{PTO} = 4.099$ Å (note that in-plane PTO polarization is favored by electrostatic alignment with slightly strained STO [40]). Interference of the $c_{PTO}$ dimension with the strong scattering DSO substrate (pseudocubic $a_{DSO} = 3.944$ Å) then yields a moiré constant of 10.4 nm, which agrees with the observation of scattering rods in the $q_x$-$q_z$ plane [37–40]. In the normal direction, interference of the $a_{PTO}$ dimensions with fully relaxed STO ($a_{STO} = 3.905$ Å) yields a moiré constant of 64.0 nm, which corresponds well with the easily overlooked scattering rods in the $q_x - q_z$ plane corresponding to a $d$ spacing of 63.8 nm (found on the STO and PTO (0 0 4) reflections of the high quality dataset in Fig. 1(a) of Stoica *et al.* [40]). Considering the mismatch between the contributing lattices offers a simple route to predict the resulting vortex superlattice dimensions. More generally, such moiré patterning could be used to induce purely structural long-range order in 2D and 3D ferroic systems, which will project the same periodicity on the corresponding electronic states. In this regard, it will be crucial to investigate and understand possible alterations of moiré periodicity with decreasing film thickness, particularly for ultrathin ($<20$ unit cells) nanolayers, where elastic compensation of the mismatch energy is expected.

In summary, we observe near perfect relaxation of a thin STO film grown on a low lattice mismatch LSAT substrate, leading to a 2D square Moiré pattern. The resulting Moiré domains with approximately 40 nm relate to a commensurate 106/107 supercell relation—an unprecedented and extraordinary observation since the periodicity here is 3–4 times larger than reported (few layer) systems and is predicted to be tunable depending on the substrate-nanolayer combination.
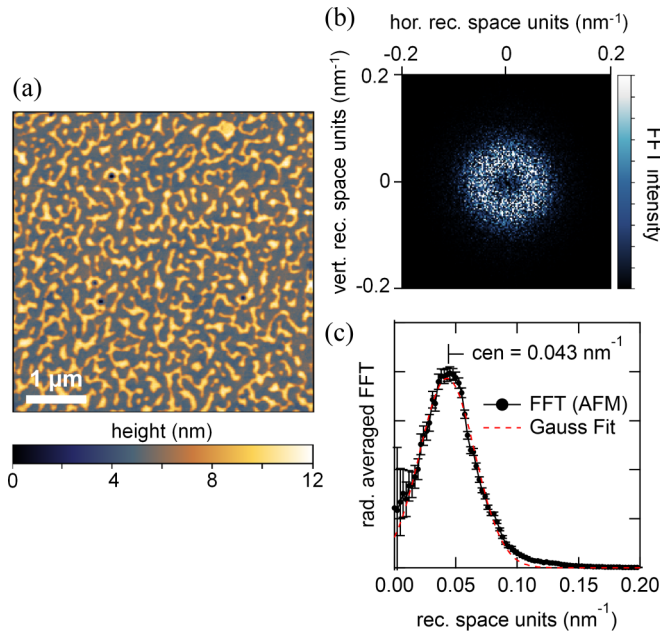
FIG. 4. (a) Atomic force microscopy (AFM) image of the SrTiO₃ (STO) surface after annealing, showing a common lateral disordered arrangement of islands. (b) Reciprocal space image of the surface morphology obtained via two-dimensional (2D) fast Fourier transform (FFT) (using Hanning window function) of the AFM image shown in (a). The radial-symmetric intensity distribution confirms no preferred alignment direction of the surface features. (c) Average of 20 radial cuts together with a Gaussian fit to quantify the mean correlation length.

This perfect lattice relaxation is based on a highly ordered 2D line dislocation network. Further, the possibility to detect and characterize the atomic order at the interface, particularly over macroscopic length scales, will be of significant interest for design and optimization of such promising heterostructured material systems. Regarding the recent and exciting observation of 3D ferroelectric vortex structures and polar supercrystals, our explanation now allows one to predict the expected polar domain sizes simply based on the atomic lattice, which will greatly facilitate the design of new 2D and 3D ferroelectric vortex geometries. Furthermore, the presence of a highly ordered dislocation network at the interface could result in 2D conductivity along the defect lines, which might open a range of unforeseen potential applications of the LSAT-STO material system.

Experimental and derived data are accessible from the PSI Public Data Repository [65].

## APPENDIX A: SURFACE ANALYSIS

For surface analysis, AFM images were acquired on a Bruker Dimension Icon Scanning Station in tapping mode, and images were analyzed using the Gwyddion package. To correct for sample nonplanarity, a sloped background (fitted polynomial) was subtracted. For correlation analysis, the AFM image was Fourier transformed using a Hanning window function for spatial filtering. Radial averaging to obtain the mean correlation length was performed by averaging 20 radial cuts (width = 4 pixels = 0.007 nm⁻¹) through the reciprocal space images, as shown in Fig. 4. Here, the peak center at $q = 0.043 \pm 0.002$ nm⁻¹ relates to a real-space mean correlation length of $2\pi/q = 146.1 \pm 7.2$ nm.

## APPENDIX B: RSV—LINE CUTS

For a more detailed analysis, we retrieved orthogonal line cuts through the RSV of the (2, 0, 2) reflection (see Fig. 2 for RSV projections). The width of each cut was 3 voxels, corresponding to 0.0015 r.l.u. in $H$-$K$-$L$-space. As shown in the out-of-plane cut in Fig. 5(a), clear layer fringes are visible, which were fit (see blue line) to obtain a film thickness of
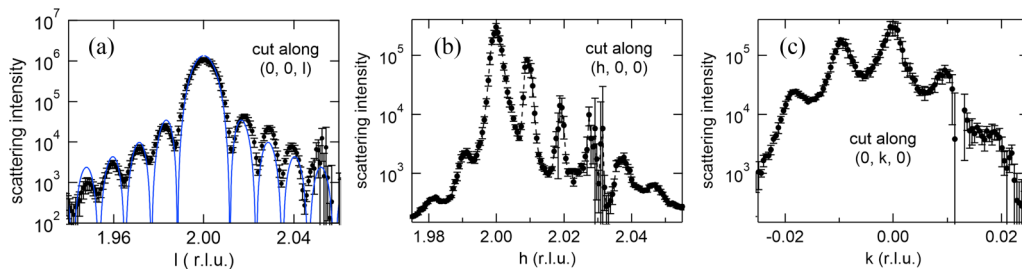


FIG. 5. Line cuts through the (2, 0, 2) reciprocal space volume (RSV; see Fig. 2) along (a) (0, 0, l), (b) (h, 0, 0), and (c) (0, k, 0). The out-of-plane fringe pattern in (a) was fitted (blue line) to obtain the film thickness of $33 \pm 2$ nm. In (b) and (c), along both directions, clear satellite peaks around the central (2, 0, 2) reflection are evident.
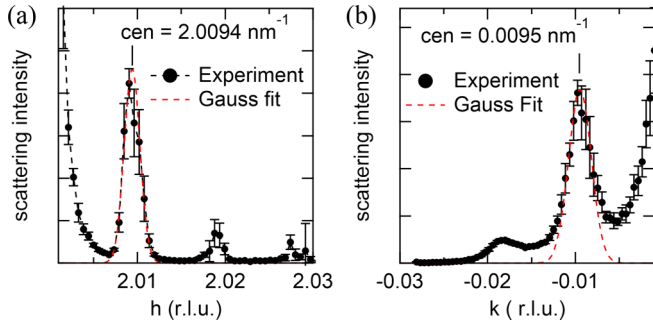
FIG. 6. Gaussian fits of the first satellite peaks seen in the horizontal line cuts along (a) $(h, 0, 0)$ and (b) $(0, k, 0)$, as shown in Figs. 5(b) and 5(c).

$33 \pm 2$ nm. Further, both in-plane cuts along the $(h, 0, 0)$ and $(0, k, 0)$ direction (see Figs. 5(b) and 5(c), respectively) show clear satellite peaks around the central $(2, 0, 2)$ reflection. Note that data points with significantly larger error bars [e.g., at $h \sim 2.03$ r.l.u. in Fig. 5(b)] stem from attenuation correction of detector images close to the LSAT substrate reflection. Here, an x-ray absorber attenuates the direct beam to avoid damaging the detector, which in turn reduces the diffuse scattering. When mapping together all images into the RSV, the recorded intensity is corrected for the primary beam attenuation, which in turn drastically amplifies counting noise in the diffuse scattering regime.

To quantify the in-plane scattering features, we fitted the first satellite peaks by a Gaussian peak function, as shown in Fig. 6. The fits show a reciprocal spacing between the main $(2, 0, 2)$ reflection and the first satellite peak of $\Delta h = 0.0094 \pm 0.0001$ r.l.u and $\Delta k = 0.0095 \pm 0.0001$ r.l.u., corresponding to a real-space $d$ spacing of $41.1 \pm 0.4$ nm. The obtained peak widths of $w_h = 0.0013 \pm 0.00007$ r.l.u. and $w_k = 0.0012 \pm 0.00015$ r.l.u. yield a coherent scattering length of $300.0 \pm 24.5$ nm, which is significantly larger than the surface morphologies seen in the AFM Fourier analysis

(see Fig. 4). By correcting the fitted peak width for broadening effects stemming from the RSV resolution (0.0005 r.l.u.), one obtains a corrected coherent scattering length of $325.4 \pm 30.1$ nm.

## APPENDIX C: 2D MODEL CALCULATIONS

To reproduce the scattering behavior from interfacial interference effects, we reduce the scenario to a 2D problem. Hence, we define 2D matrices representing artificial scattering length density (SLD) real-space grids of $300 \times 300$ nm$^2$ for LSAT (matrix A) and STO (matrix B; both: size $= 10^5 \times 10^5$ voxels, real-space resolution $= 0.03$ Å/voxel). First, we assume SLD $= 0$ for all points in both matrices. Second, we write lattices with unit cell parameters corresponding to LSAT (in matrix A) and STO (in matrix B), such that we obtain square lattices with SLD $= 1$ at the base points of the unit cells. Third, we calculate the interference matrix $I_{AB}$ by simple matrix addition—an example of such an interference matrix (here, for a $\frac{9}{10}$ base lattice) is shown in Fig. 7(a). When the base points of the lattices overlap (lattice overlap points), the SLD is increased compared with base lattice sites. However, a FFT of such a lattice [see Fig. 7(b)] does not reproduce the experimentally observed superlattice Bragg rods.

If, however, we introduce a nonzero imaginary contribution to the lattice overlap points (which is the equivalent to a phase-shifted contribution in the scattering experiment), higher order superlattice peaks appear in the reciprocal space image [see Fig. 7(c)]. Regarding the LSAT-STO material system, such a phase-shifted scattering contribution is caused by a change in out-of-plane or in-plane atomic displacement surrounding the lattice overlap points (within the *H-K* plane, reciprocal space distances between the scattering contributions are only sensitive to in-plane order, while out-of-plane order modulates the scattering intensities by altering the Fourier contributions). See Appendix D for confirmation of the corrugation-induced phase shift.
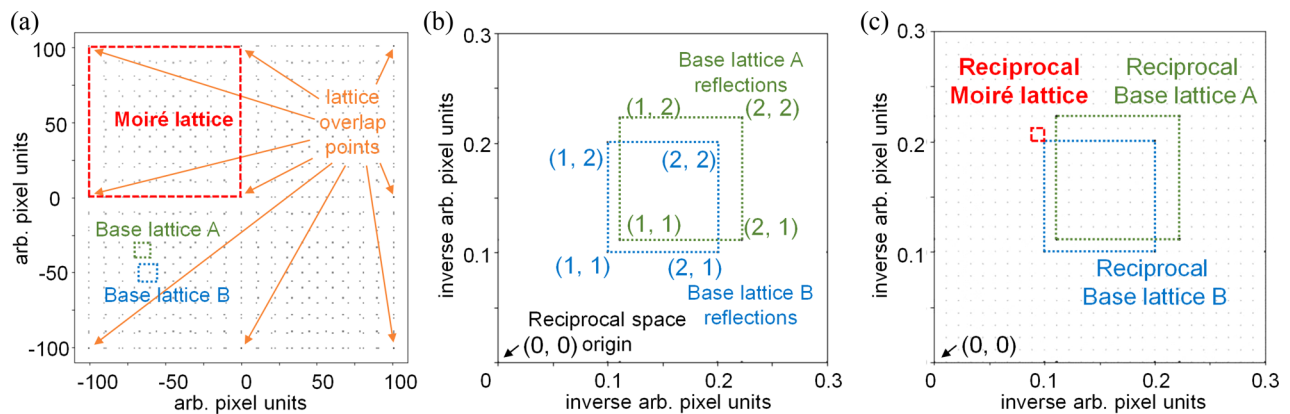


FIG. 7. (a) Real-space interference matrix $I_{AB}$ illustrating occurrence of a moiré lattice from two exemplary $\frac{9}{10}$ base lattices, as shown in green and blue. After sufficient unit cell repetitions, the two lattice base points overlap, causing an increase in the scattering length density (SLD) in our model (lattice overlap points marked by orange arrows). These overlap points reoccur in a square symmetry, which constitutes the "moiré lattice" (see red box). (b) and (c) Intensity of the fast Fourier transforms (FFTs) of the interference matrix $I_{AB}$. (b) FFT where all $I_{AB}$ matrix elements have no complex terms. Only the two reflection families stemming from the base lattices *A* and *B* (green and blue) are visible. (c) FFT where an arbitrary complex constant has been added at the overlap points shown in (a). In addition to the two base lattice reflections (green and blue), higher order contributions from the interference superstructure appear. These moiré lattice reflections are consistent with experimental observations (see Fig. 2).
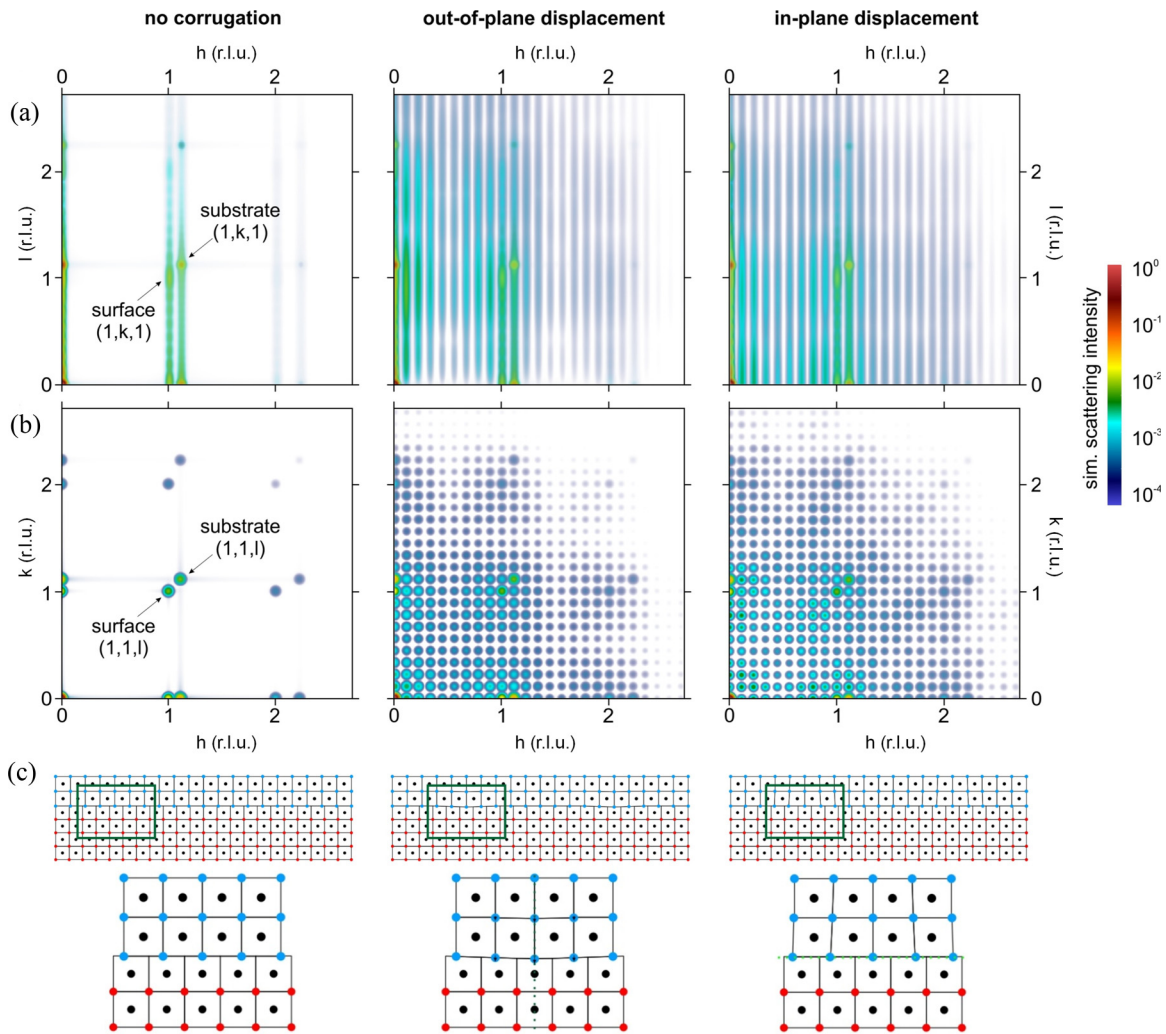
FIG. 8. Results of the three-dimensional (3D) model calculations, showing the intensity of the fast Fourier transforms (FFTs) that yield reciprocal space volumes (RSVs) along the (a) out-of-plane and (b) in-plane direction. (c) Illustrative sketches of the underlying geometries. The left column shows results from two lattices of different sizes and no out-of-plane corrugation, yielding only Bragg-like reflections that correspond to the two unit cell parameters. The middle column shows results from two lattices of different sizes and 10% out-of-plane corrugation, and the right column shows results from two lattices of different sizes and 10% in-plane atomic displacements. Here, a strong superstructure scattering contribution is observed, confirming both in- and out-of-plane corrugation as a cause for the experimentally observed scattering features.

## APPENDIX D: 3D MODEL CALCULATIONS

To investigate if atomic displacement in the form of a dislocation network can cause the scattering peaks observed in the experimental data, we perform 3D calculations on a perovskite system with reduced size. Due to the massive computational overhead of 3D FFTs, we reduce the system to a $\frac{9}{10}$ supercell geometry (note that a 3D representation of the above used 2D model would contain $10^5 \times 10^5 \times 10^5 = 10^{15}$ voxels, which would require several petabytes of random access memory). In quantitative terms, we define a matrix of $1500 \times 1500 \times 1000$ voxels ($X \times Y \times Z$), where we fill the lower $0 < z < 612$ voxels with $ABO_3$ unit cells with a lattice parameter of 18 voxels, representing the LSAT substrate. On top, we place 10 layers (from $630 < z < 830$ voxels) of $ABO_3$ unit cells with a lattice parameter of 20 voxels, representing the STO nanolayer. Hence, we have a $\frac{20}{18} = \frac{10}{9}$ supercell sys-

tem with a moiré lattice with a size of 180 voxels. Orthogonal slices through the 3D RSV obtained from FFT of this system are shown in Figs. 8(a) and 8(b)—left (the final FFT was weighted by a Gauss function). In analogy to the experimental data, the reciprocal space was scaled to $h$, $k$, and $l$ units of the surface layer.

Most evident, we observe faint rodlike scattering within the (out-of-plane) $h$-$l$ scattering plane. On the $(1, k, 1)$ substrate peak [see Fig. 8(a)], this is an FFT artefact caused by the finite length of the input matrix [note that the same effect is weaker but present within the (in-plane) $h$-$k$ plane, where the input matrix is significantly larger]. On the $(1,k,1)$ surface layer peak, the finite thickness of the surface broadens the Bragg-like scattering peak and also causes the thickness-related Laue oscillations along the $l$ direction. Within the (in-plane) $h$-$k$ plane [see Fig. 8(b)], the scattering rods appear as simple peaks—very similar to our 2D model calculations shown in

Fig. 7(b). In summary, for this case of two unit cell types with no interfacial structural effects, we only observe Bragg-like scattering corresponding to the two lattice parameters of substrate and surface.

We now induce two separate atomic displacements like the local strain field around a dislocation: (i) an out-of-plane corrugation and (ii) a radial in-plane displacement [see Fig. 3(b) for HRTEM images of such a dislocation]. For both types of displacement, we first find the position of maximal local mismatch, which occurs exactly half-way between the moiré overlap points [e.g., see Fig. 3(a)]. At this position, we assume that the strain field around the dislocation is highly localized: in-plane, it only affects unit cells up to the second next neighbor (so $\pm 40$ voxels), whereas out of plane, the strain decays with $\frac{1}{z}$ and is hence only significant in the first two layers above the substrate. The effective displacements are then calculated according to a 2D Gauss function with (a) an amplitude of 4 voxels at the point of maximal local mismatch and (b) a period of the structural moiré motif of 180 voxels [see Fig. 8(c) for a sketch of these structures compared with the nondisplaced system].

As shown in Fig. 8(a), the 3D FFT calculations of both geometries clearly show the presence of superstructure scattering in the form of Bragg rods extended along the (out of plane) $l$ direction. Noteworthy, the intensity of the superstructure scattering is stronger on the scattering plane from the surface layer (e.g., $l = 1, 2, \ldots$) than on the substrate peak. Within the (in plane) $h$-$k$ plane [see Fig. 8(b)], a squared and highly ordered superstructure lattice becomes evident. Also, here, both types of displacement induce the same superstructure periodicity. However, the in-plane intensity modulation of these superstructures is slightly different, which likely stems from a different dislocation form factor scattering (in-plane displacement changes the shape of the repetitive phase-shifting motif). In summary, for the case of two unit cell types with either in-plane or out-of-plane displacement of the surface layer close to the interface, we observe Bragg-like scattering convoluted with the superstructure scattering motif caused by the phase-shift contributions of the moiré lattice. Note that this is likely an oversimplification of the exact process.

### APPENDIX E: SrTiO₃ ON NdGaO₃

To confirm that the observed moiré motifs are not only intrinsic to the LSAT-STO material system but occur also in other material combinations, we performed the exact same heat treatment procedure on a sample of ∼25 nm STO grown
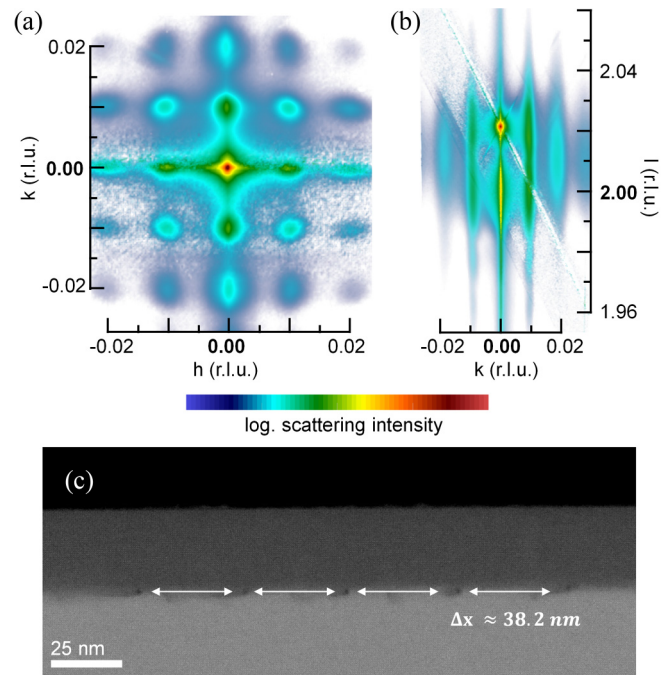


FIG. 9. (a) In-plane and (b) out-of-plane cuts through the reciprocal space volume (RSV) of the (0, 0, 2) reflection of SrTiO₃ (STO)- NdGaO₃ (NGO) sample system. Also, in this case, we observe the same moiré superstructure scattering motif as in the STO $-$ (LaAlO₃)$_{0.3}$(Sr₂TaAlO₆)$_{0.7}$(LSAT) system but with a spacing of $\Delta h = 0.0106$, relating to a real-space $d$ spacing of 36.8 nm. (c) High resolution transmission electron microscopy (HRTEM) images of a sample cross-section, showing the sample lattice dislocation pattern at the interface as for the STO-LSAT system [see Fig. 3(b)] but with a periodicity of $38.2 \pm 1.8$ nm.

on NdGaO₃ (NGO). Considering the unit cell dimensions of NGO ($a_{\mathrm{PC,NGO}} = 3.864$ Å) and STO ($a_{\mathrm{STO}} = 3.905$ Å) with a lattice mismatch of 1.21% (compare with LSAT with $a_{\mathrm{LSAT}} = 3.869$ Å and lattice mismatch of 0.93%), we expect a slightly smaller moiré motif with 37.3 nm periodicity.

Also, in this case, we performed XRD experiments to reconstruct the RSV around the (0, 0, 2) reflection (reciprocal space units are given in the STO reference system). As shown in Fig. 9, we observe the same superstructure scattering rods as in LSAT (see Figs. 1 and 2). However, here, the distance between the scattering rods is $\Delta h = 0.0106$. This corresponds to a real-space $d$ spacing of 36.8 nm, which is in excellent agreement with the expected moiré periodicity.

[1] J. Mannhart and D. G. Schlom, Oxide interfaces—an opportunity for electronics, Science **327**, 1607 (2010).

[2] M. J. Jin, S. Y. Moon, J. Park, V. Modepalli, J. Jo, S. I. Kim, H. C. Koo, B. C. Min, H. W. Lee, S. H. Baek, and J. W. Yoo, Nonlocal spin diffusion driven by giant spin Hall effect at oxide heterointerfaces, Nano Lett. **17**, 36 (2017).

[3] M. Gibert, M. Viret, A. Torres-Pardo, C. Piamonteze, P. Zubko, N. Jaouen, J. M. Tonnerre, A. Mougin, J. Fowlie, S. Catalano, A. Gloter, O. Stéphan, and J. M. Triscone, Interfacial control of magnetic properties at LaMnO₃/LaNiO₃ interfaces, Nano Lett. **15**, 7355 (2015).

[4] S. R. Lee, L. Baasandorj, J. W. Chang, I. W. Hwang, J. R. Kim, J. G. Kim, K. T. Ko, S. B. Shim, M. W. Choi, M. You, C. H. Yang, J. Kim, and J. Song, First observation of ferroelectricity in ∼1 Nm ultrathin semiconducting BaTiO₃ films, Nano Lett. **19**, 2243 (2019).

[5] T. L. Kim, M. J. Choi, T. H. Lee, W. Sohn, and H. W. Jang, Tailoring of interfacial band offsets by an atomically thin polar insulating layer to enhance the water-splitting performance of oxide heterojunction photoanodes, Nano Lett. **19**, 5897 (2019).

[6] C. W. Bark, P. Sharma, Y. Wang, S. H. Baek, S. Lee, S. Ryu, C. M. Folkman, T. R. Paudel, A. Kumar, S. V. Kalinin, A. Sokolov, E. Y. Tsymbal, M. S. Rzchowski, A. Gruverman, and C. B. Eom, Switchable induced polarization in LaAlO₃/SrTiO₃ heterostructures, Nano Lett. **12**, 1765 (2012).

[7] L. Wu, C. Li, M. Chen, Y. Zhang, K. Han, S. Zeng, X. Liu, J. Ma, C. Liu, J. Chen, J. Zhang, Ariando, T. V. Venkatesan, S. J. Pennycook, J. M. D. Coey, L. Shen, J. Ma, X. R. Wang, and C. W. Nan, Interface-induced enhancement of ferromagnetism in insulating LaMnO₃ ultrathin films, ACS Appl. Mater. Interfaces **9**, 44931 (2017).

[8] C. A. F. Vaz, F. J. Walker, C. H. Ahn, and S. Ismail-Beigi, Intrinsic interfacial phenomena in manganite heterostructures, J. Phys. Condens. Matter **27**, 123001 (2015).

[9] H. J. A. Molegraaf, J. Hoffman, C. A. F. Vaz, S. Gariglio, D. van der Marel, C. H. Ahn, and J.-M. Triscone, Magnetoelectric effects in complex oxides with competing ground states, Adv. Mater. **21**, 3470 (2009).

[10] S.-W. Cheong and M. Mostovoy, Multiferroics: A magnetic twist for ferroelectricity, Nat. Mater. **6**, 13 (2007).

[11] C. Rao, Transition metal oxides, Annu. Rev. Phys. Chem. **40**, 291 (1989).

[12] N. Reyren, S. Thiel, A. D. Caviglia, L. F. Kourkoutis, G. Hammerl, C. Richter, C. W. Schneider, T. Kopp, A.-S. Ruetschi, D. Jaccard, M. Gabay, D. A. Muller, J.-M. Triscone, and J. Mannhart, Superconducting interfaces between insulating oxides, Science **317**, 1196 (2007).

[13] M. Huijben, G. Rijnders, D. H. A. Blank, S. Bals, S. Van Aert, J. Verbeeck, G. Van Tendeloo, A. Brinkman, and H. Hilgenkamp, Electronically coupled complementary interfaces between perovskite band insulators, Nat. Mater. **5**, 556 (2006).

[14] A. Ohtomo and H. Y. Hwang, A high-mobility electron gas at the LaAlO₃/SrTiO₃ heterointerface, Nature **427**, 423 (2004).

[15] Y. Chen, R. J. Green, R. Sutarto, F. He, S. Linderoth, G. A. Sawatzky, and N. Pryds, Tuning the two-dimensional electron liquid at oxide interfaces by buffer-layer-engineered redox reactions, Nano Lett. **17**, 7062 (2017).

[16] M. A. Islam, D. Saldana-Greco, Z. Gu, F. Wang, E. Breckenfeld, Q. Lei, R. Xu, C. J. Hawley, X. X. Xi, L. W. Martin, A. M. Rappe, and J. E. Spanier, Surface chemically switchable ultraviolet luminescence from interfacial two-dimensional electron gas, Nano Lett. **16**, 681 (2016).

[17] W. Niu, Y. Zhang, Y. Gan, D. V. Christensen, M. V. Soosten, E. J. Garcia-Suarez, A. Riisager, X. Wang, Y. Xu, R. Zhang, N. Pryds, and Y. Chen, Giant tunability of the two-dimensional electron gas at the interface of $\gamma$-Al₂O₃/SrTiO₃, Nano Lett. **17**, 6878 (2017).

[18] Y. Xie, C. Bell, T. Yajima, Y. Hikita, and H. Y. Hwang, Charge writing at the LaAlO₃/SrTiO₃ surface, Nano Lett. **10**, 2588 (2010).

[19] Y. Z. Chen, J. L. Zhao, J. R. Sun, N. Pryds, and B. G. Shen, Resistance switching at the interface of LaAlO₃/SrTiO₃, Appl. Phys. Lett. **97**, 123102 (2010).

[20] P. Zubko, N. Jecklin, A. Torres-Pardo, P. Aguado-Puente, A. Gloter, C. Lichtensteiger, J. Junquera, O. Stéphan, and J.-M.

[21] Triscone, Electrostatic coupling and local structural distortions at interfaces in ferroelectric/paraelectric superlattices, Nano Lett. **12**, 2846 (2012).

[21] A. Brinkman, M. Huijben, M. van Zalk, J. Huijben, U. Zeitler, J. C. Maan, W. G. van der Wiel, G. Rijnders, D. H. A. Blank, and H. Hilgenkamp, Magnetic effects at the interface between non-magnetic oxides, Nat. Mater. **6**, 493 (2007).

[22] H. Ohta, S. Kim, Y. Mune, T. Mizoguchi, K. Nomura, S. Ohta, T. Nomura, Y. Nakanishi, Y. Ikuhara, M. Hirano, H. Hosono, and K. Koumoto, Giant thermoelectric Seebeck coefficient of a two-dimensional electron gas in SrTiO₃, Nat. Mater. **6**, 129 (2007).

[23] J. Garcia-Barriocanal, A. Rivera-Calzada, M. Varela, Z. Sefrioui, E. Iborra, C. Leon, S. J. Pennycook, and J. Santamaria, Colossal ionic conductivity at interfaces of epitaxial ZrO₂:Y₂O₃/SrTiO₃ heterostructures, Science **321**, 676 (2008).

[24] A. Soumyanarayanan, N. Reyren, A. Fert, and C. Panagopoulos, Emergent phenomena induced by spin-orbit coupling at surfaces and interfaces, Nature **539**, 509 (2016).

[25] A. Manchon, H. C. Koo, J. Nitta, S. M. Frolov, and R. A. Duine, New perspectives for Rashba spin-orbit coupling, Nat. Mater. **14**, 871 (2015).

[26] V. Sunko, H. Rosner, P. Kushwaha, S. Khim, F. Mazzola, L. Bawden, O. J. Clark, J. M. Riley, D. Kasinathan, M. W. Haverkort, T. K. Kim, M. Hoesch, J. Fujii, I. Vobornik, A. P. Mackenzie, and P. D. C. King, Maximal rashba-like spin splitting via kinetic-energy-coupled inversion-symmetry breaking, Nature **549**, 492 (2017).

[27] W. Lin, L. Li, F. Doğan, C. Li, H. Rotella, X. Yu, B. Zhang, Y. Li, W. S. Lew, S. Wang, W. Prellier, S. J. Pennycook, J. Chen, Z. Zhong, A. Manchon, and T. Wu, Interface-based tuning of Rashba spin-orbit interaction in asymmetric oxide heterostructures with 3d electrons, Nat. Commun. **10**, 3052 (2019).

[28] C. R. Dean, L. Wang, P. Maher, C. Forsythe, F. Ghahari, Y. Gao, J. Katoch, M. Ishigami, P. Moon, M. Koshino, T. Taniguchi, K. Watanabe, K. L. Shepard, J. Hone, and P. Kim, Hofstadter's butterfly and the fractal quantum Hall effect in moiré superlattices, Nature **497**, 598 (2013).

[29] K. Tran *et al.*, Evidence for moiré excitons in van der Waals heterostructures, Nature **567**, 71 (2019).

[30] J. L. Servoin, Y. Luspin, and F. Gervais, Infrared dispersion in SrTiO₃ at high temperature, Phys. Rev. B **22**, 5501 (1980).

[31] A. A. Sirenko, C. Bernhard, A. Golnik, A. M. Clark, J. Hao, W. Si, and X. X. Xi, Soft-mode hardening in SrTiO₃ thin films, Nature **404**, 373 (2000).

[32] P. Marsik, K. Sen, J. Khmaladze, M. Yazdi-Rizi, B. P. P. Mallett, and C. Bernhard, Terahertz ellipsometry study of the soft mode behavior in ultrathin SrTiO₃ films, Appl. Phys. Lett. **108**, 052901 (2016).

[33] Y. Yamada and G. Shirane, Neutron scattering and nature of the soft optical phonon in SrTiO₃, J. Phys. Soc. Jpn. **26**, 396 (1969).

[34] J. H. Haeni, P. Irvin, W. Chang, R. Uecker, P. Reiche, Y. L. Li, S. Choudhury, W. Tian, M. E. Hawley, B. Craigo, A. K. Tagantsev, X. Q. Pan, S. K. Streiffer, L. Q. Chen, S. W. Kirchoefer, J. Levy, and D. G. Schlom, Room-temperature ferroelectricity in strained SrTiO₃, Nature **430**, 758 (2004).

[35] V. Skoromets, C. Kadlec, J. Drahokoupil, J. Schubert, J. Hlinka, and P. Kužel, Systematic study of terahertz response of SrTiO₃

based heterostructures: Influence of strain, temperature, and electric field, Phys. Rev. B **89**, 214116 (2014).

[36] A. Verma, S. Raghavan, S. Stemmer, and D. Jena, Ferroelectric transition in compressively strained $SrTiO_3$ thin films, Appl. Phys. Lett. **107**, 192908 (2015).

[37] A. R. Damodaran *et al.*, Phase coexistence and electric-field control of toroidal order in oxide superlattices, Nat. Mater. **16**, 1003 (2017).

[38] A. K. Yadav, C. T. Nelson, S. L. Hsu, Z. Hong, J. D. Clarkson, C. M. Schlepuëtz, A. R. Damodaran, P. Shafer, E. Arenholz, L. R. Dedon, D. Chen, A. Vishwanath, A. M. Minor, L. Q. Chen, J. F. Scott, L. W. Martin, and R. Ramesh, Observation of polar vortices in oxide superlattices, Nature **530**, 198 (2016).

[39] S. Das *et al.*, Observation of room-temperature polar skyrmions, Nature **568**, 368 (2019).

[40] V. A. Stoica *et al.*, Optical creation of a supercrystal with three-dimensional nanoscale periodicity, Nat. Mater. **18**, 377 (2019).

[41] S. W. Lee, Y. Liu, J. Heo, and R. G. Gordon, Creation and control of two-dimensional electron gas using al-based amorphous oxides/$SrTiO_3$ heterostructures grown by atomic layer deposition, Nano Lett. **12**, 4775 (2012).

[42] M. Steins, J. Doerschel, and P. Reiche, Crystal structure of aluminium lanthanum strontium tantalum oxide, $(La_{0.272}Sr_{0.728})(Al_{0.648}Ta_{0.352})O_3$, Z. Kristallogr. NCS **212**, 77 (1997).

[43] M. Kozina, M. Fechner, P. Marsik, T. van Driel, J. M. Glownia, C. Bernhard, M. Radovic, D. Zhu, S. Bonetti, U. Staub, and M. C. Hoffmann, Terahertz-driven phonon upconversion in $SrTiO_3$, Nat. Phys. **15**, 387 (2019).

[44] Z. Huang, K. Han, S. Zeng, M. Motapothula, A. Y. Borisevich, S. Ghosh, W. Lü, C. Li, W. Zhou, Z. Liu, M. Coey, T. Venkatesan, and Ariando, The effect of polar fluctuation and lattice mismatch on carrier mobility at oxide interfaces, Nano Lett. **16**, 2307 (2016).

[45] P. R. Willmott *et al.*, The materials science beamline upgrade at the Swiss light source, J. Synchrotron Radiat. **20**, 667 (2013).

[46] B. D. Patterson, R. Abela, H. Auderset, Q. Chen, F. Fauth, F. Gozzo, G. Ingold, H. Kühne, M. Lange, D. Maden, D. Meister, P. Pattison, T. Schmidt, B. Schmitt, C. Schulze-Briese, M. Shi, M. Stampanoni, and P. R. Willmott, The materials science beamline at the Swiss light source: Design and realization, Nucl. Instrum. Methods Phys. Res. A **540**, 42 (2005).

[47] C. M. Schlepütz, S. O. Mariager, S. A. Pauli, R. Feidenhans'l, and P. R. Willmott, Angle calculations for a (2+3)-type diffractometer: Focus on area detectors, J. Appl. Crystallogr. **44**, 73 (2011).

[48] E.-J. Guo, R. Desautels, D. Keavney, M. A. Roldan, B. J. Kirby, D. Lee, Z. Liao, T. Charlton, A. Herklotz, T. Zac Ward, M. R. Fitzsimmons, and H. N. Lee, Nanoscale ferroelastic twins formed in strained $LaCoO_3$ films, Sci. Adv. **5**, eaav5050 (2019).

[49] J. G. Connell, B. J. Isaac, G. B. Ekanayake, D. R. Strachan, and S. S. A. Seo, Preparation of atomically flat $SrTiO_3$ surfaces using a deionized-water leaching and thermal annealing procedure, Appl. Phys. Lett. **101**, 251607 (2012).

[50] D. Xu, Y. Yuan, H. Zhu, L. Cheng, C. Liu, J. Su, X. Zhang, H. Zhang, X. Zhang, and J. Li, Nanostructure and optical property investigations of $SrTiO_3$ films deposited by magnetron sputtering, Materials **12**, 138 (2019).

[51] M. Radovic, N. Lampis, F. M. Granozio, P. Perna, Z. Ristic, M. Salluzzo, C. M. Schlepütz, and U. S. Di Uccio, Growth and characterization of stable SrO-Terminated $SrTiO_3$ surfaces, Appl. Phys. Lett. **94**, 022901 (2009).

[52] P. P. Ewald, Introduction to the dynamical theory of x-ray diffraction, Acta Cryst. **25**, 103 (1969).

[53] C. Nicklin, Capturing surface processes, Science **343**, 739 (2014).

[54] A. Neagu and C.-W. Tai, Local disorder in $Na_{0.5}Bi_{0.5}TiO_3$-piezoceramic determined by 3d electron diffuse scattering, Sci. Rep. **7**, 12519 (2017).

[55] G. X. Ni, H. Wang, J. S. Wu, Z. Fei, M. D. Goldflam, F. Keilmann, B. Özyilmaz, A. H. Castro Neto, X. M. Xie, M. M. Fogler, and D. N. Basov, Plasmons in graphene moiré superlattices, Nat. Mater. **14**, 1217 (2015).

[56] D. Martoccia, T. Brugger, M. Björck, C. M. Schlepütz, S. A. Pauli, T. Greber, B. D. Patterson, and P. R. Willmott, H-BN/Ru(0001) Nanomesh: A 14-on-13 superstructure with 3.5 nm periodicity, Surf. Sci. **604**, L16 (2010).

[57] P. Zeller, X. Ma, and S. Günther, Indexing moiré patterns of metal-supported graphene and related systems: Strategies and pitfalls, New J. Phys. **19**, 013015 (2017).

[58] P. Merino, M. Švec, A. L. Pinardi, G. Otero, and J. A. Martín-Gago, Strain-driven moiré superstructures of epitaxial graphene on transition metal surfaces, ACS Nano **5**, 5627 (2011).

[59] J. Narayan and B. C. Larson, Domain epitaxy: A unified paradigm for thin film growth, J. Appl. Phys. **93**, 278 (2003).

[60] M. Iannuzzi, I. Kalichava, H. Ma, S. J. Leake, H. Zhou, G. Li, Y. Zhang, O. Bunk, H. Gao, J. Hutter, P. R. Willmott, and T. Greber, Moiré beatings in graphene on Ru(0001), Phys. Rev. B **88**, 125433 (2013).

[61] D. Martoccia, M. Björck, C. M. Schlepütz, T. Brugger, S. A. Pauli, B. D. Patterson, T. Greber, and P. R. Willmott, Graphene on Ru(0001): A corrugated and chiral structure new journal of physics graphene on Ru(0001): A corrugated and chiral structure, New J. Phys. **12**, 043028 (2010).

[62] J. Santiso, J. Roqueta, N. Bagués, C. Frontera, Z. Konstantinovic, Q. Lu, B. Yildiz, B. Martínez, A. Pomar, L. Balcells, and F. Sandiumenge, Self-arranged misfit dislocation network formation upon strain release in $La_{0.7}Sr_{0.3}MnO_3$/$LaAlO_3$(100) epitaxial films under compressive strain, ACS Appl. Mater. Interfaces **8**, 16823 (2016).

[63] P. M. Anderson, J. P. Hirth, and J. Lothe, *Theory of Dislocations*, 3rd ed. (Cambridge University Press, Cambridge, 2017).

[64] K. Szot, W. Speier, G. Bihlmayer, and R. Waser, Switching the electrical resistance of individual dislocations in single-crystalline $SrTiO_3$, Nat. Mater. **5**, 312 (2006).

[65] DOI: 20.500.11935/5a1b3bc1-1b38-4755-9e8d-86b85897b50d.